

Quasiparticle Spectroscopy of Chiral Charge Order

Jiangchang Zheng,^{1,2} Caiyun Chen,^{1,2} Gaopei Pan,^{3,4,2} Xu Zhang,^{4,2} Chen Chen,¹
Yuan Da Liao,⁴ Ganesh Pokharel,^{5,6} Andrea Capa Salinas,⁵ Yizhou Wei,¹ Hoi Chun
Po,¹ Ding Pan,^{1,7} Stephen D. Wilson,⁵ Zi Yang Meng,^{4,*} and Berthold Jäck^{1,†}

¹*Department of Physics, The Hong Kong University of Science and Technology,
Clear Water Bay, Kowloon, Hong Kong SAR*

²*These authors contributed equally*

³*Institut für Theoretische Physik und Astrophysik
and Würzburg-Dresden Cluster of Excellence ct.qmat,
Universität Würzburg, 97074 Würzburg, Germany*

⁴*Department of Physics and HK Institute of Quantum Science & Technology,
The University of Hong Kong, Pokfulam Road, Hong Kong SAR*

⁵*Materials Department, University of California Santa Barbara, California 93106, USA*

⁶*Department of Natural Sciences, University of West Georgia, Carrollton, GA 30118, USA*

⁷*Department of Chemistry, The Hong Kong University of Science and Technology,
Clear Water Bay, Kowloon, Hong Kong SAR*

(Dated: March 26, 2025)

Abstract

Electronic interactions can give rise to novel charge density waves with unconventional ground states. Recent experiments report evidence for a chiral charge density wave (CDW) that breaks time-reversal symmetry in the kagome metals AV_3Sb_5 ($A=K, Rb$ or Cs). Theoretical analyses propose a topologically nontrivial loop current phase that spontaneously breaks time-reversal symmetry as the favorable CDW ground state. However, spectroscopic insights into the quasiparticle excitations of chiral charge order in AV_3Sb_5 compounds are still missing and conflicting experimental results question the presence of a loop current phase. We employed individual magnetic atoms as local quantum sensors to examine the quasiparticle excitations of chiral charge order in CsV_3Sb_5 with the scanning tunneling microscope (STM). Our spectroscopic measurements show that the magnetic moment of Co induces a spatially-localized low-energy state in the CDW phase. The distinct spectral signatures of this state are consistent with theoretical expectations for the quasiparticle excitation of a loop current order parameter, while control experiment rule out alternative scenario. Our work provides unique insights into the ground state of chiral charge order in CsV_3Sb_5 and introduces a novel method to examine other topological states, such as the fractional Chern insulators, with the STM.

A microscopic loop current at the atomic scale carries an orbital magnetic moment, which breaks time-reversal symmetry (TRS). The collective orbital magnetism of loop currents arranged on a crystal lattice has long been proposed as a mechanism to engender topologically non-trivial electronic states in materials that lack local magnetic moments [1–4]. This approach is distinct from established concepts to realize integer and fractional Chern insulators that rely on doping topological insulators with magnetic atoms [5, 6] or on the magnetic moments of localized charge carriers occupying electronic flat bands [7–15]. Hence, microscopic loop currents could impart novel topological phases of matter with potentially unique properties in a broader range of material classes.

This hitherto elusive concept has drawn renewed attention through the detection of a TRS-breaking charge density wave (CDW) in non-magnetic kagome lattice materials of the AV_3Sb_5 (where A is K, Rb or Cs) family using different experimental methods [16–22]. Theoretical analyses [23, 24] propose that charge correlations [25–27] on the kagome lattice could indeed favor the formation of the sought-after loop current phase, dubbed chiral flux phase (CFP), that spontaneously breaks TRS and hosts a set of topological bands with non-zero Chern number. This interpretation remains heavily debated, owing to conflicting results on the presence of TRS-breaking in these materials and the role external stimuli may play for the emergence of these characteristics [28–30]. From an experimental viewpoint, this controversy is rooted in the general difficulty of isolating unambiguous signatures of a static, antiferromagnetic or perfectly compensated orbital-only order parameter in measurements of the electric, magnetic, and optical material properties. Hence, further insights into the ground state of the chiral charge order demand for novel experimental approaches.

In this work, we introduce a technique to spectroscopically examine the quasiparticle excitations of the chiral charge order state in CsV_3Sb_5 with the scanning tunneling microscope (STM). Using individual magnetic Co atoms deposited to the surface of CsV_3Sb_5 as local quantum sensors (as schematically shown in Fig. 1a), we visualize a spatially localized low-energy state. The spectroscopic signatures of this state are consistent with theoretical expectations for the topological quasiparticle excitation of a loop current order parameter, which arises through the coupling between the flux sector of the loop current phase and the local magnetic moment of the Co atom.

RESULTS

Topographic and electronic properties of CsV₃Sb₅

We first establish the essential topographic and spectroscopic properties of CsV₃Sb₅ in the presence of charge correlations, which take a key role in concepts of loop current order in this material [23, 24]. CsV₃Sb₅ crystallizes in a hexagonal structure ($a = b = 5.4 \text{ \AA}$, $c = 9 \text{ \AA}$) and is composed of vanadium (V) antimony (Sb) layers that are stacked with caesium (Cs) along the crystallographic c -direction (as seen in Fig. 1, b and c) [31]. The V-Sb layer is composed of a kagome lattice of V atoms which coordinates a hexagonal lattice of Sb atoms. Fig. 1d displays the STM topography recorded on the Sb-terminated surface of a cleaved CsV₃Sb₅ crystal recorded at a temperature $T = 4 \text{ K}$. Owing to the comparably weak chemical bond between the Cs and Sb atoms, the cleaved surface is commonly terminated by the Sb layer [25].

The STM topography is characterized by the honeycomb structure of the Sb lattice, which exhibits periodic distortions (as seen in Fig. 1d). The analysis of the two-dimensional (2D) fast-Fourier transform (FFT) reveals six Bragg peaks (q_{Bragg}) that can be associated with the Sb lattice structure (as shown in Fig. 1e). The 2D-FFT also features two more sets of wave vectors, q_{4a} and $q_{2a \times 2a}$. The vector q_{4a} was previously associated with a unidirectional charge density wave (CDW), which consolidates at $T < 50 \text{ K}$ and breaks the C_{6z} symmetry of the kagome lattice [25]. The $q_{2a \times 2a}$ vector signals the presence of the $2a \times 2a$ CDW [25, 26], which arises through a $3Q$ -scattering mechanism between the crystallographic M -points of the kagome band structure [23, 24, 32] at $T < 94 \text{ K}$ [27], retains the C_{6z} symmetry, and increases the unit cell area by a factor of four. It has been proposed that the CFP could be the ground state of this $2a \times 2a$ CDW. Note that the relative intensity of the $q_{2a \times 2a}$ peaks in the 2D-FFT is strongly bias voltage-dependent owing to the strong impact of the q_{4a} CDW on the surface topography [25]. Therefore, the relative intensity of the six $q_{2a \times 2a}$ peaks at $V_B = -100 \text{ mV}$ breaks the six-fold rotation symmetry, as shown in Fig. 1d.

We conducted scanning tunneling spectroscopy (STS) measurements to characterize the local density of states of CsV₃Sb₅. The dI/dV spectrum recorded over a larger bias voltage (V_B) range (as shown in Fig. 1f) exhibits a peak (shoulder) at $V_B \approx -200 \text{ mV}$ ($V_B \approx 200 \text{ mV}$) that can be associated with van Hove singularities at the crystallographic M -point [25, 32, 33]. dI/dV spectra recorded over a smaller bias voltage range are shown in Fig. 1g. They are characterized by a pronounced V-gap feature with shoulders at $V_B \approx \pm 20 \text{ mV}$ (as indicated by black solid triangles) at the Fermi level. This "pseudogap" feature was previously identified as the spectral gap associated

with the formation of the $2a \times 2a$ CDW in real space [25, 26, 34].

Detecting the Kondo effect of individual Co atoms at the surface of $\text{Cs}(\text{V}_{0.95}\text{Ti}_{0.05})_3\text{Sb}_5$

Next, we focus on slightly titanium-doped CsV_3Sb_5 to examine the response of its electronic states to a local magnetic moment when charge correlations are absent. The partial substitution of vanadium with titanium effectively hole-dopes the electron systems. It was previously reported that titanium doping with $x > 0.05$ shifts the van Hove singularity of the kagome band structure away from the Fermi energy, resulting in a suppression of the $2a \times 2a$ CDW [35]. We examined $\text{Cs}(\text{V}_{0.95}\text{Ti}_{0.05})_3\text{Sb}_5$ samples with $x = 0.05$ Ti doping. A 2D-FFT analysis of STM topographies recorded on the surface of these samples is presented in Sec. 1 of the Suppl. Materials. In agreement with previous results [36], this analysis confirms the absence of the $2a \times 2a$ and $4a$ CDWs at this doping level. Moreover, the topographic appearance of the Ti dopants is strongly bias voltage dependent. As shown in Sec. A of the Suppl. Materials, clear topographic signatures of Ti atoms can only be detected at large bias voltages $|V_B| = 1$ V. At $|V_B| \leq 0.5$ V, only smooth variations of the topographic background can be detected. Note that dI/dV spectra recorded on the surface of $\text{Cs}(\text{V}_{0.95}\text{Ti}_{0.05})_3\text{Sb}_5$ samples lack the V-shaped pseudogap previously detected on undoped CsV_3Sb_5 (as seen in Fig. 2a). This suggests the absence of charge correlations in $\text{Cs}(\text{V}_{0.95}\text{Ti}_{0.05})_3\text{Sb}_5$, in agreement with earlier reports [35].

Co atoms were evaporated on the cold ($T = 4$ K) surface of $\text{Cs}(\text{V}_{0.95}\text{Ti}_{0.05})_3\text{Sb}_5$ (see Methods section). Figure 2b shows an STM topography after the deposition of Co atoms. This topography was recorded at a bias voltage $V_B = -0.5$ V in order to suppress topographic features associated with the Ti dopants. Note the absence of the $q_{2a \times 2a}$ peaks in the 2D-FFT (inset of Fig. 2b). The Co atoms are distributed across the surface and can be distinguished from other randomly occurring surface defects by a characteristic star-of-David (SoD) shape. We highlight one Co atom by a white dashed circle in Fig 2a. The bright white dots correspond to Cs atoms adsorbed to the sample surface [25]. Note that we detect small variations in the topographic appearance of the SoD shape that presumably result from variations of the electronic background due to Ti doping. Interestingly, the Co atoms do not assume ad-atomic positions on top of the sample surface. Instead, they integrate into the surface layer as indicated by their vanishing apparent topographic height. The analysis of the close-up view (as shown by yellow dashed lines in Fig. 2c) indicates that the Co atoms always reside at the center of the honeycomb lattice of the Sb atoms (*c.f.* Fig. 1c). Consistent with this experimental observation, our results from *ab-initio* simulations

on the surface adsorption process of Co atoms support their integration into the honeycomb center of the top-most Sb layer, as shown in Sec. B of the Supplementary Materials.

We conducted STS measurements to characterize the response of $\text{Cs}(\text{V}_{0.95}\text{Ti}_{0.05})_3\text{Sb}_5$ to the presence of individual Co atoms. dI/dV spectra recorded at, near and away from the Co atom position (as shown in Fig. 2d) are presented in Fig. 2b. The dI/dV spectra recorded at and far away from the Co-atom position are comparable and dominated by a reduction of the dI/dV amplitude near Fermi energy E_F . Interestingly, the dI/dV spectrum (red solid line) recorded one unit cell away from the Co atom exhibits a pronounced peak at $V_B \approx -5$ mV. The off-center-position of this dI/dV peak can be clearly seen in spectroscopic mapping measurements. dI/dV maps recorded at the bias voltage of this peak exhibit a circular enhancement of the dI/dV amplitude around the Co atom position (as shown in Fig. 2e). This halo-like enhancement of the dI/dV -amplitude is most pronounced at $V_B = -5$ mV and all but absent at $V > 0$ mV (as seen in Fig. 2f). We show dI/dV maps recorded at other bias voltages, as well as additional data sets that reproduce these results in Sec. C of the Suppl. Materials. Note that all Co atoms deposited on the surface of $\text{Cs}(\text{V}_{0.95}\text{Ti}_{0.05})_3\text{Sb}_5$ exhibit this dI/dV peak at $V_B < 0$ despite small variations in the topographic characteristics of the SoD pattern.

These observations suggest the presence of the Kondo effect in $\text{Cs}(\text{V}_{0.95}\text{Ti}_{0.05})_3\text{Sb}_5$ induced by the magnetic moment of the Co atom. To experimentally verify this hypothesis, we characterized the temperature dependence of the dI/dV peak recorded on the exact same Co atom (as shown in Fig. 2g). Increasing the experimental temperature continuously from 4 to 24 K increases its spectral width Γ . Our analysis shows that this broadening effect cannot be solely explained by thermal broadening $\Gamma \propto k_B T$. Instead, the temperature-dependent dI/dV peak can be better described with a Fano line shape using least-square fits (shown in Fig. 2g). Details and accuracy of the fitting procedure are described in Sec. D of the Suppl. Materials. The extracted temperature dependence of Γ follows the well-known Kondo expression $\Gamma(T) = \sqrt{\pi(k_B T)^2 + 2(k_B T_K)^2}$ (as shown in Fig. 2h), which is bounded by the intrinsic spectral width of the Kondo resonance for $T \rightarrow 0$ K (k_B and T_K denote Boltzman's constant and the and Kondo temperature, respectively) [37]. We can accurately reproduce this temperature-dependent Fano line shape analysis using data recorded on another Co atom, as shown in Sec. D of the Suppl. Materials.

The Kondo effect characteristics depend on the local orbital coupling of the magnetic impurity and its environment [38]. The reproducible phenomenology of the Kondo effect observed in our measurements is consistent with the observation that the Co atoms deposited on the surface of $\text{Cs}(\text{V}_{0.95}\text{Ti}_{0.05})_3\text{Sb}_5$ assume identical positions in the honeycomb center of the topmost Sb layer. It

is also noteworthy that the halo-shape distribution of the spectral weight of the Kondo resonance in real space (as seen in Fig. 2e) is consistent with the sub-surface position of the Co-atom, as reported previously [39]. Meanwhile, the asymmetric Lorentzian shape of the Fano resonance (as seen in Fig. 2b) suggests a significant degree of electron tunneling from the STM tip into the Co $3d$ -orbitals [37, 40]. This finding agrees with our results from ab-initio calculations that suggest a Co atom position in the top-most Sb-layer (shown in Sec. 2 of the Suppl. Materials), such that tunneling into the $3d$ -orbital of Co can occur. Note that our attempts to manipulate the position of the Co atoms with the STM tip failed, probably owing to its sub-surface position within the top-most Sb-layer. The experimental observation of the Kondo effect indicates that the Co-atoms residing within the top-most Sb-layer retain their magnetic moment when deposited on the surface of Ti-doped CsV_3Sb_5 .

Visualizing the localized quasiparticle excitations of CsV_3Sb_5 induced by a local magnetic moment

We now examine the response of charge correlations in CsV_3Sb_5 to the local magnetic moment of a Co atom. To this end, we evaporated Co atoms onto the cold surface of undoped CsV_3Sb_5 (as shown in Fig. 3a), which exhibits the characteristic $2a \times 2a$ and $4a$ CDWs, respectively. The Co atoms are randomly distributed across the sample surface. Consistent with our observations on Ti-doped CsV_3Sb_5 , they exhibit SoD topographic characteristics, and the analysis of their spatial position (as shown in Fig. 3b) demonstrates their integration into the top-most Sb-layer at the honeycomb center position. These observations indicate that Co atoms deposited on the surface of doped and undoped CsV_3Sb_5 exhibit the same orbital bond structure as on the Ti-doped sample studied before.

dI/dV spectra recorded on the sample surface away from the Co atom position (black dot in Fig. 3c) feature the pseudogap near E_F (as shown in Fig. 3d) associated with the presence of the $2a \times 2a$ CDW. Spectra recorded one unit cell away from the Co atom position (red dot in Fig. 3c) additionally exhibit a pronounced dI/dV peak at $V_B \approx -5$ mV. The spectral weight of this peak is distributed in a halo-like structure in real space (as can be seen in Fig. 3f). This observation is consistent with results on $\text{Cs}(\text{V}_{0.95}\text{Ti}_{0.05})_3\text{Sb}_5$ and indicates the presence of the Kondo effect induced by the magnetic moment of the Co atom in CsV_3Sb_5 .

Interestingly, when the STM tip is located right at the Co atom position (blue dot in Fig. 3c), we detect one additional dI/dV peak that appears inside the pseudogap at positive bias voltage

$V_B \approx 10$ mV (blue solid line in Fig. 3d; the peak is highlighted by a black arrow). This dI/dV peak is particularly apparent in the difference spectrum $\Delta_{\text{norm}} dI/dV = [dI/dV(\text{Co atom position}) - dI/dV(\text{bare surface})]$ between the spectrum recorded on the Co atom position and on the bare surface (inset of Fig. 3d). dI/dV maps (shown in Fig. 3, e-i) recorded in the same field of view as Fig. 3c establish that the spectral weight of this dI/dV peak is predominantly localized at the Co atom position at the honeycomb center of the Sb lattice. This contrasts with the halo-like appearance of the Kondo effect around the Co atom position. Crucially, spectral weight of this dI/dV peak is strongest at $V_B > 0$ mV, and it can only be detected inside the pseudogap $V < 20$ mV; however, no spectral weight can be detected at energies outside the pseudogap (as shown in Fig. 3i for $V_B = 30$ mV). We reproducibly detect one dI/dV peak at $V_B > 0$ inside the pseudogap whose spectral weight is localized at the Co atom position on all examined Co atoms that were deposited on different CsV_3Sb_5 samples. Additional data sets are shown in Sec. E of the Suppl. Materials.

Next, we analyzed the profile of the spectral weight distribution of this dI/dV peak in real space (as shown in Fig. 3j) and find that it exhibits strongly anisotropic characteristics; it extends for over one nanometer along one direction of an in-plane lattice vector but remains localized to the Co atom position along any other direction. This observation indicates that the quasiparticle state, giving rise to this dI/dV peak in our measurements shown in Fig. 3d, breaks the C_{6z} symmetry of the underlying kagome lattice. At the same time, for a subset of adsorbed Co atoms, we find that the spatial distribution of the dI/dV peak does not break C_{6z} (as shown in Sec. F of the Suppl. Materials). This observation suggests that this quasiparticle excitation is not related to the $4a$ CDW that also breaks C_{6z} (*c.f.* Fig. 1d). Moreover, as we will show below, these distinct symmetry properties arise from different adsorption sites of the Co atoms within the $2a \times 2a$ CDW unit cell.

Hence, our combined observations demonstrate that the magnetic moment of Co induces a spatially localized low-energy quasiparticle excitation within the pseudogap of CsV_3Sb_5 when the $2a \times 2a$ CDW is present (as shown in Fig. 3), while this state cannot be detected when this CDW is absent (as shown in Fig. 2).

Control Experiments to rule out competing mechanisms

We further strengthen the experimental link between this quasiparticle state and the presence of a magnetic moment by conducting a set of control experiments using nonmagnetic surface

adsorbates. In fact, spectral in-gap excitations, as detected in spectroscopic measurements with the STM, can generally occur in topologically trivial charge density wave materials [41, 42] as well as in semiconductors [43, 44] and insulators [45] through the Coulomb potential of atomic-scale impurities [46–48] that effectively causes a simple impurity state. Even in the case where the ground state is topologically non-trivial, a local Coulomb potential could localize a quasiparticle state [46–51].

To rule out these scenarios, we conducted a set of control experiments that are described in detail in Sec. G of the Suppl. Materials. We examined the response of the electronic states of CsV₃Sb₅ at low energies to a range of non-magnetic surface impurities. We recorded dI/dV spectra on naturally abundant Cs adatoms and carbon monoxide molecules adsorbed to the sample surface. Moreover, we also examined the effect of individual vanadium atoms that were intentionally deposited on the sample surface (see Methods section). All these impurities are considered to be non-magnetic; the non-magnetic character of the adsorbed vanadium atoms is confirmed through the absence of the Kondo effect. According to our spectroscopic measurements shown in Sec. 8 of the Suppl. Materials, none of these adsorbate species induces a low-energy dI/dV peak inside the pseudogap that is localized at or near the impurity site in real space. Hence, the results of our control experiments rule out scenarios in which the observed low-energy dI/dV peak is associated with a simple impurity bound state caused by a local Coulomb potential. This conclusion is also consistent with the expectation that the metallic bands of CsV₃Sb₅ would efficiently screen any Coulomb potential caused by an impurity.

Topological quasiparticle excitation of loop current order

Our observations indicate that the spatially localized dI/dV peak arises through the local interaction between the atomic-scale magnetic moment of Co with the chiral CDW. To account for this effect at the theoretical level, we implement a mean-field tight-binding Hamiltonian.

$$H = H_0 + H_C = -t \sum_{\langle i,j \rangle} (\hat{c}_i^\dagger \hat{c}_j + h.c.) - \lambda \sum_p \hat{O}_p, \quad (1)$$

where H_0 accounts for the electronic nearest neighbor hopping with $t = 1$ on the kagome lattice (as shown in Fig. 4a). The coupling term $H_C = -\lambda \sum_p \hat{O}_p$ introduces a mean-field order parameter \hat{O}_p at the honeycomb center of the kagome lattice (with index p). \hat{O}_p gives rise to the local flux structure of the CFP model (and therefore the Chern bands) and drives the correct CFP current pattern on the bonds via $\hat{O}_p = i \left(\hat{c}_1^\dagger \hat{c}_2 - \hat{c}_2^\dagger \hat{c}_3 + \hat{c}_3^\dagger \hat{c}_4 + \hat{c}_4^\dagger \hat{c}_5 - \hat{c}_5^\dagger \hat{c}_6 + \hat{c}_6^\dagger \hat{c}_1 \right) + h.c.$, following the

direction of the current. Therefore, at $\lambda \neq 0$, \hat{O}_p enlarges the unit cell by a factor of four, realizing the $2a \times 2a$ CDW structure, as seen in Fig. 1, d and e. We find with $\lambda = 0.3$, $H = H_0 + H_C$ successfully reproduces the CFP state and underlying topological electronic Chern bands described by Feng *et al.* [23] (as shown in shown in Sec. H of the Supplementary Materials) in which the current direction on the kagome lattice alternates along the translation vectors. The local current directions are schematically shown in Fig. 4a.

The introduction of the local magnetic moment of Co disrupts the uniform flux pattern of the CFP. In analogy to Lenz's law, it is natural to expect that the CFP responds to this process by adjusting the local flux structure near the Co site to screen this additional magnetic moment. At a model level, this response of the CFP can be understood as a local modulation of \hat{O}_p in the presence of a static local magnetic moment. We implemented this modulation by continuously varying λ at one honeycomb lattice site x from 0.6 to -0.3 and examine the resulting eigenstate spectra of H shown in in Fig. 4b. As can be seen, the response to a weak order parameter modulation $\lambda_x > 0$, including $\lambda_x > 0.3$, (case of weak external perturbation) leaves the spectrum qualitatively unchanged. Only when the modulation of \hat{O}_p changes sign at $\lambda_x < 0$, a quasiparticle excitation deep inside the gap of the topological Chern bands appears. This spectral excitation manifests in a pronounced in-gap peak in the calculated local density of states (LDOS) (see Fig. 4c for $\lambda_x = -0.3$) consistent with our experimental observations (as shown in Fig. 3d). A local order parameter modulation with $\lambda_x < 0$ flips the sign of \hat{O}_x and, thus, results in a local reversal of the loop current order, as shown in Fig. 4d. Hence, the response of the CFP to screen an atomic-scale magnetic moment of sufficient amplitude induces a local flux defect in the loop current order.

We further computed the wavefunction content of the quasiparticle excitation created by a flux defect ($\lambda_x = -0.3$) as shown in Fig. 4, e and f. The spectral weight of the in-gap excitation is strongly localized near the defect site. Moreover, in agreement with our experimental observations shown in Fig. 3, h and j, we find two scenarios. When the flux defect is placed in a subset (labeled 2-4 in Fig. 4d) of the four plaquettes of the $2a \times 2a$ CDW unit cell, the wavefunction breaks the underlying C_{6z} symmetry of the kagome lattice by extending predominantly along one spatial direction. Breaking C_{6z} results from the local reversal of the current directions surrounding the position of the flux defect, as can be seen in Fig. 4d. On the other hand, the wavefunction of the local quasiparticle excitation preserves C_{6z} , as shown in Fig. 4f, when the defect is placed at the high-symmetry site of the CDW unit cell (labelled 1). Overall, the results of this theoretical analysis in the framework of a CFP model qualitatively and even quantitatively agree with the experimental observations presented in Fig. 3.

DISCUSSION

Our combined experimental observations, control experiments, and theoretical analyses suggest that the coupling between the magnetic moment of a single Co-atom and the orbital magnetization of the loop current phase in CsV_3Sb_5 creates a localized quasiparticle excitation within the topologically non-trivial gap of the underlying Chern band [23, 24]. On the other hand, the topological trivial CBO state has been suggested as an alternative ground state of the chiral charge order in AV_3Sb_5 [23, 24]. Unlike the loop current phase, the CBO does not spontaneously break time-reversal symmetry. Hence, the local interaction of a magnetic moment and a CBO is of Zeeman type. We have calculated the effect of a local magnetic moment on the CBO by considering a local Zeeman term H_Z at plaquette i using $H = H_{\text{CBO}} + H_Z = H_{\text{CBO}} + \kappa(n_{i,\uparrow} - n_{i,\downarrow})$ where H_{CBO} denotes the Hamiltonian of the CBO as defined in Ref. [23] and κ the strength of the Zeeman effect. As shown in Sec. I of the Suppl. Materials, the presence of a local Zeeman term induces two eigenstates of comparable amplitude inside the CDW gap in the calculated local density of states. Moreover, the spectral weight of these in-gap states exhibits a nonuniform real-space distribution around the plaquette site and breaks all spatial symmetries. These characteristics can be clearly distinguished from our experimental observations presented in Fig. 3 that show one in-gap state at $V_B > 0$ whose real space spectral weight distributions have C_{6z} or C_{2z} symmetry. Therefore, our experimental results are incompatible with a pure CBO state and suggest the presence of a spontaneously TRS breaking loop current phase in the ground state of the chiral charge order. This is in agreement with previous results from optical Kerr rotation and nuclear magnetic resonance measurements [19, 52]. Note that this loop current phase (imaginary part) could appear as a part of a complex-valued order parameter including the CBO (real part) as discussed recently [22, 30, 53].

The magnetic moment of the loop current order was found to have an upper bound of $\leq 0.02 \mu_B$ (μ_B denotes the Bohr magneton) according to muon spin relaxation measurements [54]. Given a local quasiparticle excitation that reverses a current loop carries a comparable moment, we expect a negligible magnetic field B induced Zeeman shift E_z/B on the order of $E_z/B \leq 1 \mu\text{eV}/\text{T}$. We tested the response of this low-energy dI/dV peak to a magnetic field $B = \pm 1 \text{ T}$ applied along the out-of-plane direction, as shown in Sec. J of the Suppl. Materials. In agreement with this estimate, we cannot detect any spectral changes in this in-gap state at $V_B > 0$ upon application of B . The magnetic field also does not affect the Kondo dI/dV peak at $V_B < 0$; note that we are also unable to detect a B -induced change in the chirality of the CDW, as previously reported [16, 22]. It has been suggested that impurities hinder the field-induced switching of the CDW chirality [16, 55],

and we hypothesize that the presence of Co atoms disfavors the switching of the CDW chirality in our measurements.

Our theoretical model captured by Eq. (1), in particular, the local response of the loop current order parameter to the atomic-scale magnetic moment comes with strong physical intuition. It is worthwhile to elaborate further on the connection between the theoretical model and the experimental observation, as follows. From a microscopic perspective, the modulation of the loop current order parameter on a hexagon in Eq. (1), can be generated by the local magnetic exchange interactions between the spin S_p^z of the Co atom and the magnetic moment of the current loop on that hexagon in the form of $J_{i,i+1}^z S_p^z$ term where $J_{i,i+1}^z = i(\hat{c}_i^\dagger \hat{c}_{i+1} - \hat{c}_{i+1}^\dagger \hat{c}_i)$ is the current operator between site $i, i + 1$. As derived in Sec. K of the Suppl. Materials, this local magnetic moment-current coupling has the same order as the linear moment S_p^z part of the Kondo local magnetic moment-onsite coupling and, in concert with magnetic anisotropy effects at the sample surface [56, 57], stabilizes a preferred direction of the magnetic moment of the Co atom [58]. This understanding is consistent with the reproducible observation of the in-gap state at $V_B \approx 10$ mV in the dI/dV spectra recorded on all examined Co atoms. Moreover, the spontaneous TRS-breaking leaves one spin flavor in the mean field Hamiltonian (as in the case of the quantum anomalous Hall effect) and gives the local current imaginary part that facilitates the creation of the flux defect with a localized quasiparticle excitation, as detected in our measurements.

The physical interpretation of this excitation within the gaps of the topological Chern bands of the CFP (*c.f.* Fig. 4b) becomes evident by comparing our results with the archetypal Haldane model [1], which is a two-band version of the CFP model on the honeycomb lattice. Our theoretical analyzes, described in detail in Sec. L of the Suppl. Materials, show that the creation of a local flux defect, which is equivalent to a defect with $\lambda_x < 0$ in the CFP model of Eq. (1), results in the reversal of the local current around the defect site. The insertion of such a flux defect, in our experiment realized through the Kondo-type coupling of the magnetic moment of Co to the current loop phase, can thus be understood as the local introduction of a mass term of opposite sign at the honeycomb site of the defect. Accordingly, this process induces a chiral fermionic mode whose wave function content is localized to the defect site. At a spectral level, this mode manifests as a topological quasiparticle excitation inside the non-trivial bulk gap in agreement with our experimental observations and theoretical analyses shown in Fig. 3 and Fig. 4, respectively.

To conclude, our measurements provide the first spectroscopic insights into the quasiparticle excitations of the chiral charge order in CsV_3Sb_5 . The observation of a localized quasiparticle excitation at low energies induced by the magnetic moment of a cobalt atom suggests the presence

of a TRS-breaking loop current phase and cannot be explained by other ground states proposed for this CDW, such as a pure CBO state [23, 24], according to our theoretical analyses. More broadly, the coupling between a local magnetic moment and the flux sector of topological ground states—a manifestation of Lenz’s law at the atomic scale—discovered in this study offers new avenues to examine other interesting quantum phases of matter. We foresee that this and related methods could also reveal new insights into the fractional Chern insulator states of moiré and graphene superlattices [8–15, 59–61].

* zymeng@hku.hk

† bjaeck@ust.hk

- [1] F. D. M. Haldane, *Physical review letters* **61**, 2015 (1988).
- [2] T. Hsu, J. Marston, and I. Affleck, *Physical Review B* **43**, 2866 (1991).
- [3] C. Varma, *Physical Review B* **55**, 14554 (1997).
- [4] S. Chakravarty, R. Laughlin, D. K. Morr, and C. Nayak, *Physical Review B* **63**, 094503 (2001).
- [5] C.-Z. Chang, J. Zhang, X. Feng, J. Shen, Z. Zhang, M. Guo, K. Li, Y. Ou, P. Wei, L.-L. Wang, et al., *Science* **340**, 167 (2013).
- [6] C.-Z. Chang, C.-X. Liu, and A. H. MacDonald, *Reviews of Modern Physics* **95**, 011002 (2023).
- [7] M. Serlin, C. Tschirhart, H. Polshyn, Y. Zhang, J. Zhu, K. Watanabe, T. Taniguchi, L. Balents, and A. Young, *Science* **367**, 900 (2020).
- [8] F. Wu, T. Lovorn, E. Tutuc, I. Martin, and A. MacDonald, *Physical review letters* **122**, 086402 (2019).
- [9] P. J. Ledwith, G. Tarnopolsky, E. Khalaf, and A. Vishwanath, *Physical Review Research* **2**, 023237 (2020).
- [10] A. Abouelkomsan, Z. Liu, and E. J. Bergholtz, *Physical review letters* **124**, 106803 (2020).
- [11] H. Li, U. Kumar, K. Sun, and S.-Z. Lin, *Physical Review Research* **3**, L032070 (2021).
- [12] T. Devakul, V. Crépel, Y. Zhang, and L. Fu, *Nature communications* **12**, 6730 (2021).
- [13] H. Park, J. Cai, E. Anderson, Y. Zhang, J. Zhu, X. Liu, C. Wang, W. Holtzmann, C. Hu, Z. Liu, et al., *Nature* **622**, 74 (2023).
- [14] F. Xu, Z. Sun, T. Jia, C. Liu, C. Xu, C. Li, Y. Gu, K. Watanabe, T. Taniguchi, B. Tong, et al., *Physical Review X* **13**, 031037 (2023).
- [15] Z. Lu, T. Han, Y. Yao, A. P. Reddy, J. Yang, J. Seo, K. Watanabe, T. Taniguchi, L. Fu, and L. Ju, *Nature* **626**, 759 (2024).
- [16] Y.-X. Jiang, J.-X. Yin, M. M. Denner, N. Shumiya, B. R. Ortiz, G. Xu, Z. Guguchia, J. He, M. S. Hossain, X. Liu, et al., *Nature materials* **20**, 1353 (2021).
- [17] C. Mielke III, D. Das, J.-X. Yin, H. Liu, R. Gupta, Y.-X. Jiang, M. Medarde, X. Wu, H. C. Lei, J. Chang, et al., *Nature* **602**, 245 (2022).

- [18] R. Khasanov, D. Das, R. Gupta, C. Mielke III, M. Elender, Q. Yin, Z. Tu, C. Gong, H. Lei, E. T. Ritz, et al., *Physical Review Research* **4**, 023244 (2022).
- [19] Y. Xu, Z. Ni, Y. Liu, B. R. Ortiz, Q. Deng, S. D. Wilson, B. Yan, L. Balents, and L. Wu, *Nature physics* **18**, 1470 (2022).
- [20] Q. Wu, Z. Wang, Q. Liu, R. Li, S. Xu, Q. Yin, C. Gong, Z. Tu, H. Lei, T. Dong, et al., *Physical Review B* **106**, 205109 (2022).
- [21] C. Guo, C. Putzke, S. Konyzheva, X. Huang, M. Gutierrez-Amigo, I. Errea, D. Chen, M. G. Vergniory, C. Felser, M. H. Fischer, et al., *Nature* **611**, 461 (2022).
- [22] Y. Xing, S. Bae, E. Ritz, F. Yang, T. Birol, A. N. Capa Salinas, B. R. Ortiz, S. D. Wilson, Z. Wang, R. M. Fernandes, et al., *Nature* pp. 1–7 (2024).
- [23] X. Feng, K. Jiang, Z. Wang, and J. Hu, *Science bulletin* **66**, 1384 (2021).
- [24] M. M. Denner, R. Thomale, and T. Neupert, *Physical Review Letters* **127**, 217601 (2021).
- [25] H. Zhao, H. Li, B. R. Ortiz, S. M. Teicher, T. Park, M. Ye, Z. Wang, L. Balents, S. D. Wilson, and I. Zeljkovic, *Nature* **599**, 216 (2021).
- [26] Z. Wang, Y.-X. Jiang, J.-X. Yin, Y. Li, G.-Y. Wang, H.-L. Huang, S. Shao, J. Liu, P. Zhu, N. Shumiya, et al., *Physical Review B* **104**, 075148 (2021).
- [27] H. Li, G. Fabbris, A. Said, J. Sun, Y.-X. Jiang, J.-X. Yin, Y.-Y. Pai, S. Yoon, A. R. Lupini, C. Nelson, et al., *Nature communications* **13**, 6348 (2022).
- [28] D. R. Saykin, C. Farhang, E. D. Kountz, D. Chen, B. R. Ortiz, C. Shekhar, C. Felser, S. D. Wilson, R. Thomale, J. Xia, et al., *Physical Review Letters* **131**, 016901 (2023).
- [29] C. Farhang, J. Wang, B. R. Ortiz, S. D. Wilson, and J. Xia, *Nature Communications* **14**, 5326 (2023).
- [30] C. Guo, G. Wagner, C. Putzke, D. Chen, K. Wang, L. Zhang, M. Gutierrez-Amigo, I. Errea, M. G. Vergniory, C. Felser, et al., *Nature Physics* **20**, 579 (2024).
- [31] B. R. Ortiz, L. C. Gomes, J. R. Morey, M. Winiarski, M. Bordelon, J. S. Mangum, I. W. Oswald, J. A. Rodriguez-Rivera, J. R. Neilson, S. D. Wilson, et al., *Physical Review Materials* **3**, 094407 (2019).
- [32] M. Kang, S. Fang, J.-K. Kim, B. R. Ortiz, S. H. Ryu, J. Kim, J. Yoo, G. Sangiovanni, D. Di Sante, B.-G. Park, et al., *Nature Physics* **18**, 301 (2022).
- [33] B. R. Ortiz, S. M. Teicher, Y. Hu, J. L. Zuo, P. M. Sarte, E. C. Schueller, A. M. Abeykoon, M. J. Krogstad, S. Rosenkranz, R. Osborn, et al., *Physical Review Letters* **125**, 247002 (2020).
- [34] K. Nakayama, Y. Li, T. Kato, M. Liu, Z. Wang, T. Takahashi, Y. Yao, and T. Sato, *Physical Review B* **104**, L161112 (2021).
- [35] Y. Liu, Y. Wang, Y. Cai, Z. Hao, X.-M. Ma, L. Wang, C. Liu, J. Chen, L. Zhou, J. Wang, et al., *Physical Review Materials* **7**, 064801 (2023).
- [36] H. Yang, Z. Huang, Y. Zhang, Z. Zhao, J. Shi, H. Luo, L. Zhao, G. Qian, H. Tan, B. Hu, et al., *Science Bulletin* **67**, 2176 (2022).
- [37] K. Nagaoka, T. Jamneala, M. Grobis, and M. Crommie, *Physical review letters* **88**, 077205 (2002).
- [38] P. Wahl, L. Diekhöner, M. Schneider, L. Vitali, G. Wittich, and K. Kern, *Physical review letters* **93**,

- 176603 (2004).
- [39] H. Prüser, M. Wenderoth, P. E. Dargel, A. Weismann, R. Peters, T. Pruschke, and R. G. Ulbrich, *Nature Physics* **7**, 203 (2011).
- [40] N. Knorr, M. A. Schneider, L. Diekhöner, P. Wahl, and K. Kern, *Physical review letters* **88**, 096804 (2002).
- [41] B. Hildebrand, C. Didiot, A. M. Novello, G. Monney, A. Scarfato, A. Ubaldini, H. Berger, D. Bowler, C. Renner, and P. Aebi, *Physical review letters* **112**, 197001 (2014).
- [42] I. Lutsyk, K. Szalowski, P. Krukowski, P. Dabrowski, M. Rogala, W. Kozłowski, M. Le Ster, M. Piskorski, D. A. Kowalczyk, W. Rys, et al., *Nano Research* **16**, 11528 (2023).
- [43] A. Richardella, P. Roushan, S. Mack, B. Zhou, D. A. Huse, D. D. Awschalom, and A. Yazdani, *science* **327**, 665 (2010).
- [44] D. Edelberg, D. Rhodes, A. Kerelsky, B. Kim, J. Wang, A. Zangiabadi, C. Kim, A. Abhinandan, J. Ardelean, M. Scully, et al., *Nano letters* **19**, 4371 (2019).
- [45] R. J. P. Román, F. J. C. Costa, A. Zobelli, C. Elias, P. Valvin, G. Cassabois, B. Gil, A. Summerfield, T. S. Cheng, C. J. Mellor, et al., *2D Materials* **8**, 044001 (2021).
- [46] J. Lu, W.-Y. Shan, H.-Z. Lu, and S.-Q. Shen, *New Journal of Physics* **13**, 103016 (2011).
- [47] R.-J. Slager, L. Rademaker, J. Zaanen, and L. Balents, *Physical Review B* **92**, 085126 (2015).
- [48] S.-S. Diop, L. Fritz, M. Vojta, and S. Rachel, *Physical Review B* **101**, 245132 (2020).
- [49] V. Venkatachalam, A. Yacoby, L. Pfeiffer, and K. West, *Nature* **469**, 185 (2011).
- [50] A. Luican-Mayer, M. Kharitonov, G. Li, C.-P. Lu, I. Skachko, A.-M. B. Gonçalves, K. Watanabe, T. Taniguchi, and E. Y. Andrei, *Physical review letters* **112**, 036804 (2014).
- [51] B. E. Feldman, M. T. Randeria, A. Gyenis, F. Wu, H. Ji, R. J. Cava, A. H. MacDonald, and A. Yazdani, *Science* **354**, 316 (2016).
- [52] D. Song, L. Zheng, F. Yu, J. Li, L. Nie, M. Shan, D. Zhao, S. Li, B. Kang, Z. Wu, et al., *Science China Physics, Mechanics & Astronomy* **65**, 247462 (2022).
- [53] H. Li, Y. B. Kim, and H.-Y. Kee, *Physical Review Letters* **132**, 146501 (2024).
- [54] E. M. Kenney, B. R. Ortiz, C. Wang, S. D. Wilson, and M. J. Graf, *Journal of Physics: Condensed Matter* **33**, 235801 (2021).
- [55] S. Nakazawa, R. Tazai, Y. Yamakawa, S. Onari, and H. Kontani, *arXiv preprint arXiv:2503.07015* (2025).
- [56] F. Donati, Q. Dubout, G. Autès, F. Patthey, F. Calleja, P. Gambardella, O. V. Yazyev, and H. Brune, *Physical review letters* **111**, 236801 (2013).
- [57] I. G. Rau, S. Baumann, S. Rusponi, F. Donati, S. Stepanow, L. Gagnaniello, J. Dreiser, C. Piamonteze, F. Nolting, S. Gangopadhyay, et al., *Science* **344**, 988 (2014).
- [58] Y. Yayon, V. Brar, L. Senapati, S. Erwin, and M. Crommie, *Physical review letters* **99**, 067202 (2007).
- [59] H. Lu, B.-B. Chen, H.-Q. Wu, K. Sun, and Z. Y. Meng, *Phys. Rev. Lett.* **132**, 236502 (2024), URL <https://link.aps.org/doi/10.1103/PhysRevLett.132.236502>.

- [60] H. Lu, H.-Q. Wu, B.-B. Chen, K. Sun, and Z. Yang Meng, Reports on Progress in Physics **87**, 108003 (2024), URL <https://dx.doi.org/10.1088/1361-6633/ad7640>.
- [61] X.-Y. Song and T. Senthil, Physical Review B **110**, 085120 (2024).

FIGURES

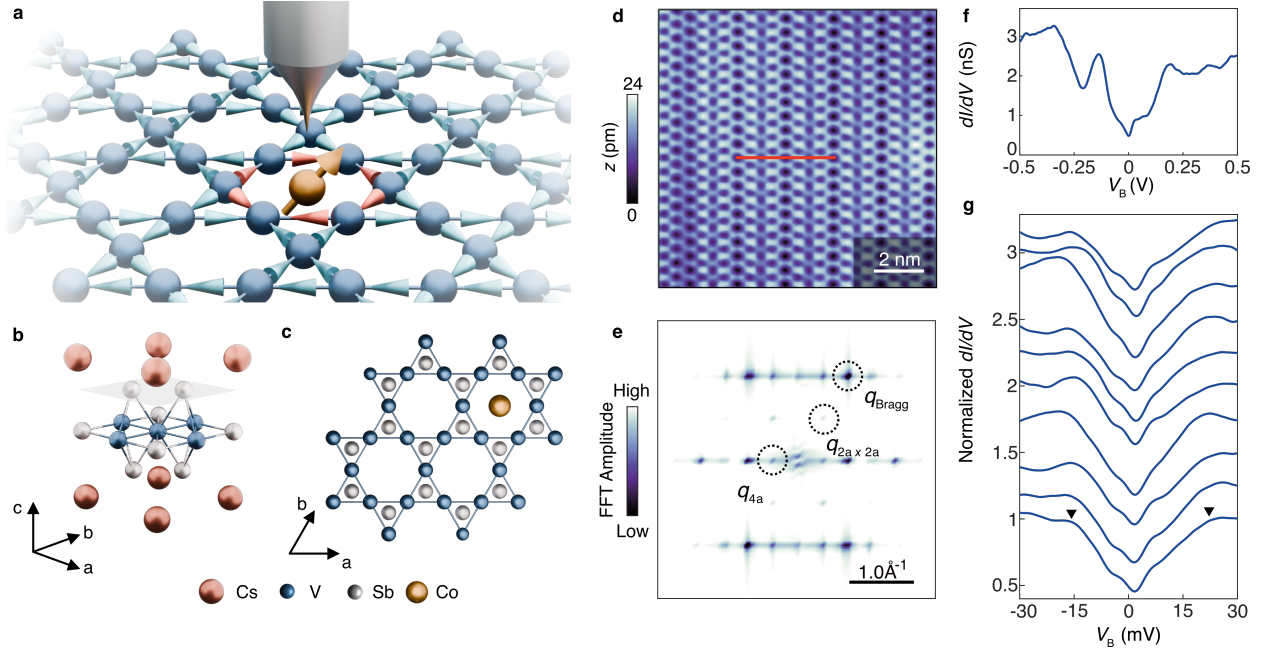


FIG. 1: **Sensing Microscopic Loop Currents in CsV_3Sb_5 with Individual Magnetic Atoms \mathbf{a} ,** Schematic presentation of the key experimental result and method. Shown is the reversal of the local loop current (red color) in the chiral flux phase (blue arrows) on the kagome lattice (blue spheres) around the adsorption site of an atomic-scale magnetic moment (orange sphere with arrow). This local loop current reversal results in a local quasiparticle excitation that can be detected with the tip of a scanning tunneling microscope (STM) as displayed. **b**, Isometric projection of the unit cell of CsV_3Sb_5 . **c**, Lattice structure of CsV_3Sb_5 along the $a - b$ plane, as seen in topographic measurements of the Sb-terminated surface with the STM. The adsorption position of the Co atom in the center of the honeycomb lattice of Sb atoms is shown. **d**, Topography of the Sb-terminated surface of CsV_3Sb_5 recorded with an STM ($V_B = -100$ mV, $I = 2$ nA, $T = 4$ K). **e**, Two-dimensional fast-Fourier transform of the topography shown in panel d. The wave vectors of the Bragg points, as well as the $2a \times 2a$ and $4a$ CDWs are indicated. **f**, Differential tunnel conductance (dI/dV) spectrum recorded on the Sb-terminated surface of CsV_3Sb_5 ($V_B = -0.5$ V, $I = 2$ nA, $V_m = 1$ mV, $T = 4$ K). **g**, Shown is a series of dI/dV spectra recorded along the red line in panel d over a smaller bias voltage range ($V_B = -30$ mV, $I = 2$ nA, $V_m = 1$ mV, $T = 4$ K). The solid triangle marks the shoulders of the V-shaped gap associated with the $2a \times 2a$ CDW.

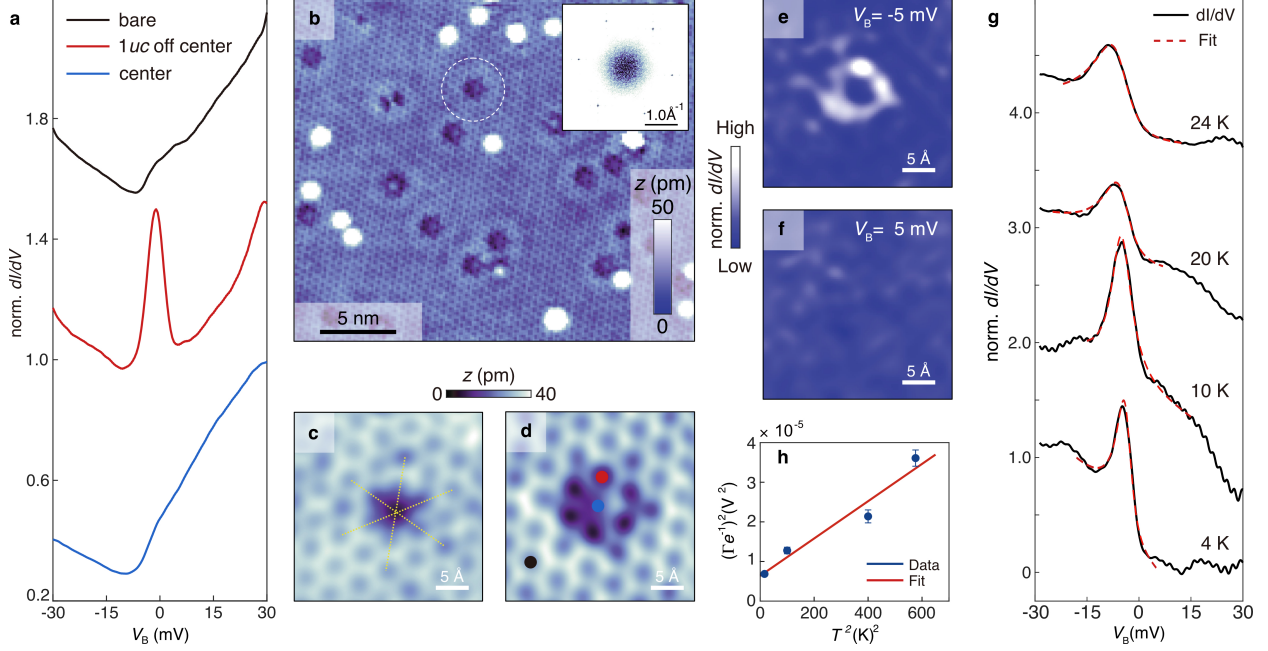


FIG. 2: Kondo Effect of Single Co Atoms at the Surface of $\text{Cs}(\text{V}_{0.95}\text{Ti}_{0.05})_3\text{Sb}_5$. **a**, Normalized dI/dV spectra recorded on the bare $\text{Cs}(\text{V}_{0.95}\text{Ti}_{0.05})_3\text{Sb}_5$ surface, one unit cell (uc) away from the Co atom position, and centered at the Co atom position. The spectra are offset by 0.5 for clarity ($V_B = -30$ mV, $I = 3$ nA, $V_m = 1$ mV, $T = 4$ K). **b**, STM topography of the Sb-terminated surface of $\text{Cs}(\text{V}_{0.95}\text{Ti}_{0.05})_3\text{Sb}_5$ after the Co atom deposition ($V_B = -0.5$ V, $I = 2$ nA, $T = 4$ K). One Co atom is highlighted by the white dashed circle. The inset displays the corresponding 2D-FFT where bright (dark) color correspond to high (low) amplitudes. **c** STM topography of a Co atom position. The yellow dashed lines indicate the position of the Co atom the center of the Sb honeycomb lattice ($V_B = 0.5$ V, $I = 2$ nA, $T = 4$ K). **d**, STM topography of the Co atom position in panel c recorded at a different bias voltage ($V_B = -0.5$ V, $I = 2$ nA, $T = 4$ K). **e** and **f**, Two-dimensional maps of the dI/dV amplitude recorded in the field of view of panel d at $V_B = -5$, and 5 mV, respectively ($I = 4$ nA, $V_m = 1$ mV, $T = 4$ K). **g**, Normalized dI/dV spectra (solid lines) recorded one unit cell away from the Co atom position (red dot in panel d) at different indicated temperatures on the exact same Co atom ($V_B = -30$ mV, $I = 2$ nA, $V_m = 1$ mV). The spectra are offset by unity and Fano line shape fits are shown as dashed lines. The comparability of the temperature-dependent dI/dV spectra recorded at different temperatures is maintained by ensuring the absence of tip changes through slow temperature change rates and spectroscopic control measurements (not shown). **h**, Displayed is the dependence of the Fano line width Γ , as extracted from the least-square fits to the dI/dV spectra shown in panel g, on the temperature T , as well as a linear least-square fit to the data points (red line). e denotes the electron charge.

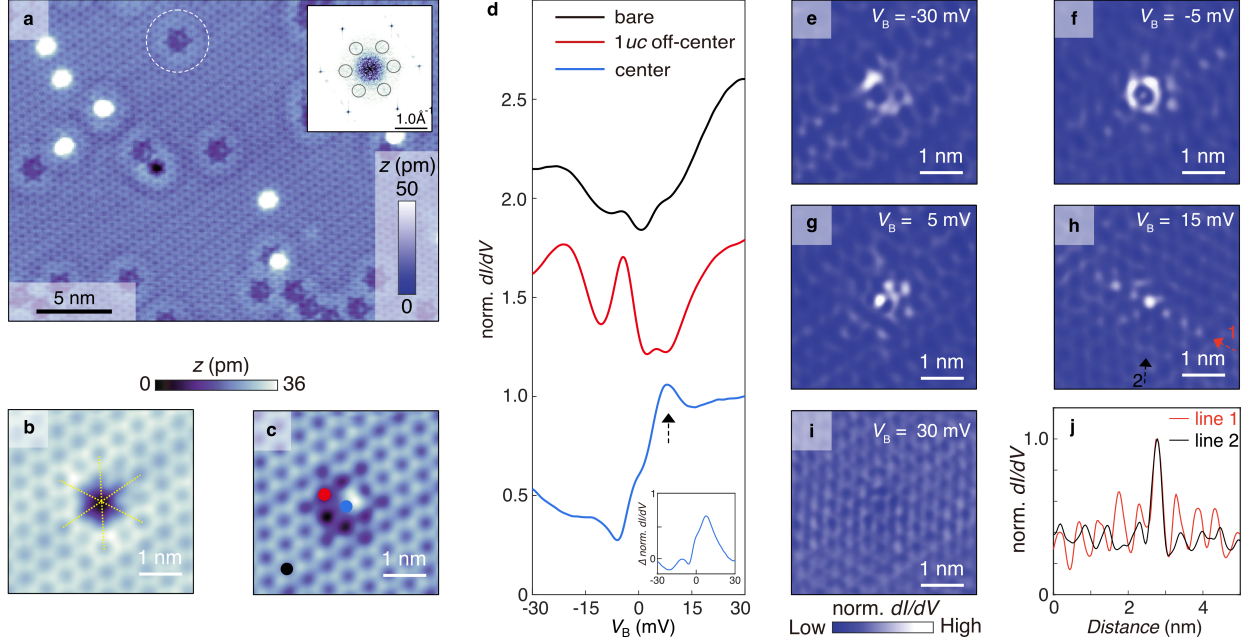


FIG. 3: Visualizing the Low-Energy Quasiparticle Excitations of CsV_3Sb_5 at the Atomic Scale

a, STM topography of the Sb-terminated surface of CsV_3Sb_5 after the Co atom deposition ($V_B = -0.5$ V, $I = 2$ nA, $T = 4$ K). The inset displays the corresponding 2D-FFT where bright (dark) color correspond to high (low) amplitudes. The positions of the $2a \times 2a$ quasiparticle interference (QPI) peaks are indicated by black circles. Owing to the bias voltage dependence of the topographic contrast, the QPI peaks have a small amplitude at $V_B = -0.5$ V [25]. **b**, STM topography of a Co atom position. The yellow dashed lines indicate the position of the Co atom the center of the Sb honeycomb lattice ($V_B = -0.5$ V, $I = 2$ nA, $T = 4$ K). **c**, STM topography of the Co-atom position in panel b recorded at a different bias voltage ($V_B = 0.5$ V, $I = 2$ nA, $T = 4$ K). **d**, Normalized dI/dV spectra recorded on the bare CsV_3Sb_5 surface, one unit cell (uc) away from the Co atom position, and centered at the Co atom position. The STM tip position is indicated by color-coded dots in panel c. The spectra are offset by unity ($V_B = -30$ mV, $I = 3$ nA, $V_m = 1$ mV, $T = 4$ K). The inset shows the difference spectrum $\Delta \text{norm. } dI/dV$ as the difference between the normalized dI/dV spectra recorded at the Co atom position (blue dot in panel c) and on the bare surface (black dot in panel c). **e-i**, shown are two-dimensional maps of the dI/dV amplitude recorded in the same field of view as panel c at $V_B = -30, -5, 5, 15,$ and 30 mV ($I = 4$ nA, $V_m = 1$ mV, $T = 4$ K). **j**, shown is the spatial dependence of the dI/dV amplitude across the Co atom position along two spatial directions. The two directions are indicated by color-coded arrows in panel h.

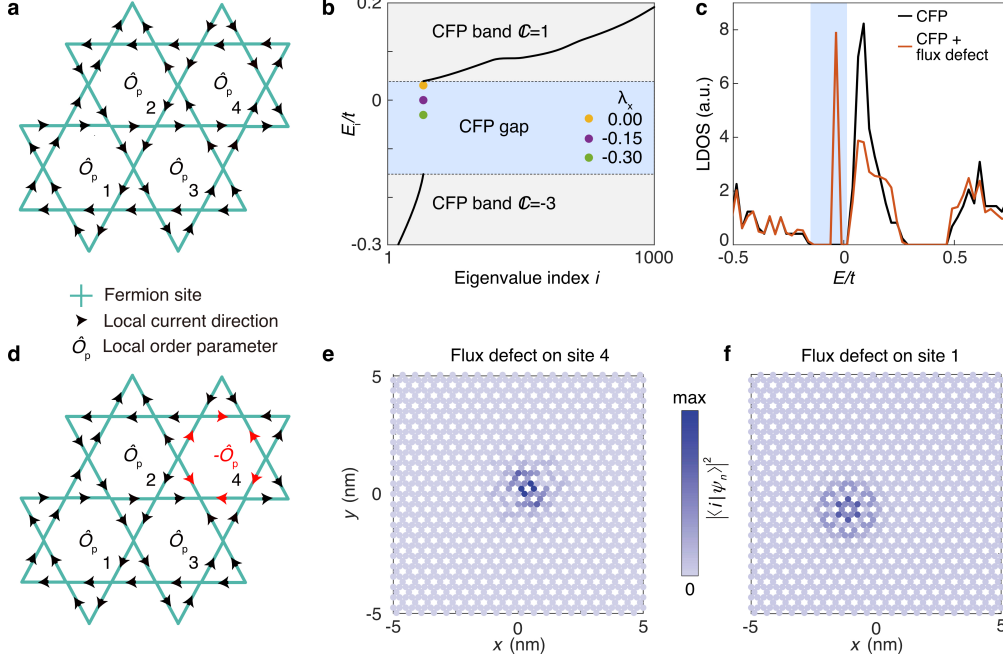


FIG. 4: Topological Quasiparticle Excitations of a Loop Current Order Parameter. **a**, Schematic representation of the CFP with local loop current order on the kagome lattice. The local current direction is indicated by black arrows and defines a local mean-field order parameter \hat{O}_p on each honeycomb plaquette of the kagome lattice. **b**, Eigenstate E_i spectrum normalized to the hopping amplitude t plotted as a function of the eigenvalue index i . The Chern bands of the CFP in the unperturbed and weakly perturbed ($0 < \lambda_x \leq 0.3$) case are shown as solid black lines and the relevant Chern numbers are indicated. The additional spectral in-gap excitations that appear in the presence of strong local order parameter perturbations are shown as color-coded dots. The spectral gap is highlighted by light blue color. **c**, Shown is the computed local density of states (LDOS) with (red line) and without (blue line) a local flux defect ($\lambda_x = -0.3$) near the flux defect position. **d**, Schematic representation of the CFP with local loop current order and a local flux defect ($\lambda_x < 0$) that changes the sign of the order parameter \hat{O}_p from positive to negative and reverses the local loop current around the defect site (as highlighted by red arrows). The spectral gap is highlighted by light blue color. **e** and **f**, shown are the real-space spectral weight distributions of the LDOS of the spectral in-gap quasiparticle excitation ($\lambda_x = -0.3$) when the flux defect is placed on plaquettes 1 and 4 of the $2a \times 2a$ CDW unit cell, respectively (numerical labels are defined in panel a).

METHODS

Synthesis of (Ti-doped) CsV_3Sb_5 crystals

Single crystals of CsV_3Sb_5 and $\text{Cs}(\text{V}_{0.95}\text{Ti}_{0.05})_3\text{Sb}_5$ were grown via a conventional flux-based growth technique. Vanadium powder purchased from the Sigma-Aldrich was cleaned using a mixture of isopropyl alcohol and Hydrochloric acid to remove residual oxides. Cs (liquid, Alfa 99.98%), V (powder, Sigma 99.9%), Ti (powder, Alfa 99.9%), and Sb (shot, Alfa 99.999%) were loaded inside a milling vial with the required stoichiometries and then sealed in an Argon-atmosphere. To grow the single crystals of $\text{Cs}(\text{V}_{1-x}\text{Ti}_x)_3\text{Sb}_5$ ($x=0, 0.05$), elemental stoichiometries, respectively, taken as $\text{Cs}_{20}\text{V}_{15-x}\text{Ti}_x\text{Sb}_{120}$ ($x=0, 3$) and then milled for about an hour. After milling, the powders were poured into the alumina crucibles and sealed inside a stainless steel tube. The samples were heated at 1000°C for 10 h and then cooled to 900°C at 25°C/hr . Below 900°C , the samples were cooled at 1°C/hr to 500°C . Once the growth period was over, the plate-like single crystals were separated gently from the flux and then cleaned with ethanol.

Scanning Tunneling Microscopy (STM) Measurements

The undoped and titanium-doped CsV_3Sb_5 samples were cleaved after cooling down to a temperature $T = 4\text{K}$ inside an ultra-high vacuum (UHV) chamber with a base pressure of $p \approx 1.4 \times 10^{-10}$ mbar. Several crystals of doped and undoped CsV_3Sb_5 were cleaved and the results presented in this manuscript were consistently observed. An electron-beam evaporator (Focus GmbH) was used to deposit cobalt and vanadium atoms from high-purity wire (99.99%) onto the samples held at $T = 4\text{K}$ inside the scanning tunneling microscope (STM). STM measurements were conducted using a home-built STM instrument under cryogenic ($4\text{K} \leq T \leq 24\text{K}$) and UHV ($p \approx 1.4 \times 10^{-10}$ mbar) conditions using a chemically etched tungsten tip. The tip was prepared on a Cu(111) surface through field emission and controlled indentation, as well as calibrated against the Cu(111) Shockley surface state before each set of measurements. Bias voltage (V) dependent differential conductance (dI/dV) spectra and maps were recorded using standard lock-in methods with a bias modulation $1\text{mV} \leq V_m \leq 10\text{mV}$ at a frequency $f = 3.971\text{kHz}$, as indicated in the main text. The dI/dV maps were recorded using multi-pass mode to avoid set-point effects.

ACKNOWLEDGMENTS

We gratefully acknowledge valuable discussions with Xi Dai and Bent Weber. This work was primarily supported by the Hong Kong RGC (Grant Nos. 26304221, 16302422, and C6033-22G) and the Croucher Foundation (Grant No. CIA22SC02) awarded to B.J and Z.Y.M (HKU C7037- 22GF). Z.Y.M. acknowledges support by the Hong Kong RGC (Grant Nos. AoE/P701/20, 17309822, 17302223), the ANR/RGC Joint Research Scheme sponsored by the Hong Kong RGC and the French National Research Agency (Project No. A HKU703/22). G.P. acknowledges support from the Würzburg-Dresden Cluster of Excellence on Complexity and Topology in Quantum Matter - ct.qmat (EXC 2147, Project No. 390858490). S.D.W., G.P., and A.C.S. gratefully acknowledge support via the UC Santa Barbara NSF Quantum Foundry funded via the Q-AMASE-i program under award DMR-1906325. D.P. acknowledges support by the National Natural Science Foundation of China through the Excellent Young Scientists Fund (Grant No. 22022310). H.C.P. acknowledge support of the National Key R&D Program of China (Grants No.2021YFA1401500), the Hong Kong RGC (Grant No. 26308021), and the Croucher Foundation (Grant No. CF21SC01). C.Y.C. acknowledges support from the Tin Ka Ping Foundation.

AUTHOR CONTRIBUTIONS

B.J., C.Y.C., and J.Z. conceived the project. J.Z. and C.Y.C. conducted the scanning tunnelling microscopy measurements and analyzed the experimental data. G.P., X.Z., Y.D.L. and Z.Y.M. designed the theoretical model and carried out the computation and discussed with B.J. on the comparison with experimental data. G.P., A.C.S., and S.D.W. synthesized the samples used in the study. C.C. and D.P. performed density functional theory calculations. All authors discussed the results and contributed to the writing of the manuscript.

COMPETING INTEREST DECLARATION

The authors declare no competing financial interest.

DATA AVAILABILITY STATEMENT

Replication data for this study can be accessed on Zenodo via link XXX.